

A solid state spin-wave quantum memory for time-bin qubits

Mustafa Gündoğan,¹ Patrick M. Ledingham,^{1,*} Kutlu Kutluer,¹
Margherita Mazzerà,^{1,†} and Hugues de Riedmatten^{1,2}

¹*ICFO-Institut de Ciències Fotoniques, Mediterranean Technology Park, 08860 Castelldefels (Barcelona), Spain*

²*ICREA-Institució Catalana de Recerca i Estudis Avançats, 08015 Barcelona, Spain*

(Dated: January 27, 2023)

We demonstrate a solid-state spin-wave optical quantum memory with on-demand read-out in a $\text{Pr}^{3+}:\text{Y}_2\text{SiO}_5$ crystal. Using the full atomic frequency comb scheme, we store weak coherent pulses at the single-photon level with a signal to noise ratio > 10 . Narrow-band spectral filtering based on spectral hole burning in a second $\text{Pr}^{3+}:\text{Y}_2\text{SiO}_5$ crystal is used to filter out the excess noise created by control pulses to reach an unconditional noise level of $(2.0 \pm 0.3) \times 10^{-3}$ photons per pulse. We also report spin-wave storage of photonic time-bin qubits with conditional fidelities higher than a classical measure and prepare strategy, demonstrating that the spin-wave memory operates in the quantum regime. These results represent an important step for the use of solid-state quantum memories in scalable quantum networks.

PACS numbers: 03.67.Hk, 42.50.Gy, 42.50.Md

Photonic quantum memories are essential in quantum information science (QIS) where they are used as quantum interfaces between flying and stationary qubits. They enable the synchronization of probabilistic quantum processes e.g. in quantum communication [1, 2] and computing [3]. The implementation of quantum memories (QMs) for light requires strong interactions between individual photons and matter. This can be achieved by placing individual quantum systems (e.g. single atoms) in high finesse cavities [4] or by using ensembles of atoms, where the photons are mapped onto collective atomic excitations. Atomic systems are natural candidates as QMs [5–12], but solid state systems offer interesting perspectives for scalability and integration into existing technology [13–19].

Rare-earth ion doped solids are promising candidates for high performance solid state QMs since they have excellent coherence properties at cryogenic temperatures [20]. They also exhibit large static inhomogeneous broadening of the optical transitions which can be tailored and used as a resource for various storage protocols, e.g. enabling temporally [21] and spectrally [22] multiplexed quantum memories. Recent experimental progress includes qubit storage [13, 22–25], highly efficient quantum storage of weak coherent states [14], storage of entangled and single photons [15, 16, 26], entanglement between two crystals [27] and quantum teleportation [28].

Yet, nonclassical states have so far only been stored as collective optical atomic excitations with fixed storage times [15, 16, 26]. While this may provide a useful resource if combined with massive multiplexing and deterministic quantum light sources [22], the ability to read-out the stored state on demand is essential for applications where the quantum memory is used as a synchronizing device. On demand read-out can be achieved by actively controlling the optical collective excitations [14], with a storage time limited by the coherence of ex-

cited states. Another solution is to transfer the optical excitations to long lived collective spin excitations (or spin-waves), using strong control pulses [29–31]. This gives access to much longer storage times [32, 33]. Operating a solid state spin-wave memory in the quantum regime has so far remained elusive, because of insufficient signal-to-noise ratio (SNR) at the single photon level [31].

Here, using the full atomic frequency comb (AFC) protocol in a $\text{Pr}^{3+}:\text{Y}_2\text{SiO}_5$ crystal we store and retrieve weak coherent pulses on-demand with $\text{SNR} > 10$ for single-photon-level input. Using a narrowband filter based on spectral hole burning in a second crystal, we achieve an unconditional noise floor of $(2.0 \pm 0.3) \times 10^{-3}$ photons per pulse. Finally, we demonstrate storage and retrieval conditional fidelities (i.e., assuming that a photon was reemitted) higher than classical memories for time-bin qubits at the single-photon level, taking into account the Poissonian statistics and the finite efficiency of the memory. These results represent the first demonstration of a solid state spin-wave quantum memory, enabling on-demand read-out of the stored qubits. They also provide the first example of a spin-wave quantum memory for time-bin qubits (for any system), an essential resource in quantum communication [34] and processing [35].

The AFC technique [13, 21] is based on spectral tailoring of an inhomogeneously broadened absorption line into a comb-shaped structure with periodicity Δ . The input pulses resonant with the comb are mapped onto a collective optical atomic excitation. After an initial dephasing, the excitations rephase at a time $1/\Delta$ giving rise to a forward collective emission [13, 21]. Before the coherent emission two strong control pulses are applied to transfer the excitation to and from a long-lived ground state to achieve the spin-wave storage of the input pulses. The full AFC scheme requires ions with at least three ground states, one being used as auxiliary state for optical pumping (see Supplemental material). The spin-wave storage

efficiency is given by $\eta_{SW} = \eta_{AFC} \times \eta_T^2 \times \eta_C$, where η_{AFC} is the efficiency of the storage at the excited state and depends on the optical depth and comb finesse [21], η_C accounts for the decoherence during the ground state storage, and η_T is the transfer efficiency of the control pulses.

The realization of the full AFC scheme in the single-photon regime is challenging as the strong control pulses create noise which may dominate the weak signal retrieved from the memory. Two main mechanisms are responsible for this noise. i) Spatial leakage from the control mode into the input mode due to scattering from the optical surfaces and ii) interaction of the control pulses with residual population in the spin storage state due to imperfect optical pumping. The latter includes collective effects, such as free-induction decay (FID), or incoherent fluorescent emission. To reduce the noise we employ spatial, temporal and spectral filtering. The spectral filtering is challenging in $\text{Pr}^{3+}:\text{Y}_2\text{SiO}_5$, as the input and control frequencies are separated by only 10.2 MHz (see Fig. 1(b)). As a narrow-band spectral filter we use a second $\text{Pr}^{3+}:\text{Y}_2\text{SiO}_5$ crystal where we prepare spectral holes of variable width [36, 37].

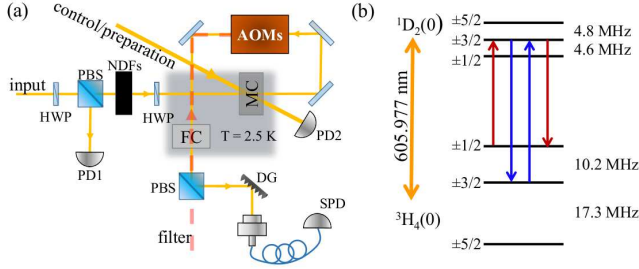


FIG. 1: (a) **Quantum memory setup.** The memory (MC) and filter (FC) crystals are located inside a liquid-free cooler (Oxford V14) operating at a temperature of 2.5 K. They are both 3 mm long and doped with a Pr^{3+} concentration of 0.05 %. The control and input beams are steered towards the memory with an angle of $\sim 1.5^\circ$, leading to an extinction ratio of 10^{-5} . The beam diameters on the crystal are $280 \mu\text{m}$ and $90 \mu\text{m}$ for strong and input modes, respectively. The weak coherent states are prepared by attenuating bright pulses with variable neutral density filters (NDFs). A portion of the input beam is picked up before the NDF and sent to a photodiode (PD1) for the calibration of the mean photon number per pulse. A mechanical shutter is used to protect the SPD during the memory and filter preparation. HWP: half-wave plate; AOM: acousto-optical modulator; DG: diffraction grating; SPD: single-photon detector. The dashed red beam indicates the filter preparation mode. (b) Hyperfine splitting of the first sublevels of the ground $^3\text{H}_4(0)$ and the excited $^1\text{D}_2$ manifold of Pr^{3+} in Y_2SiO_5 .

The experimental arrangement and the relevant energy level scheme of Pr^{3+} at 606 nm are shown in Fig. 1. The main laser beam at 606 nm (Toptica TA-SHG pro) is split into three to be used as input mode, fil-

ter preparation, and lastly for control pulses and memory preparation. They all pass through acousto-optical modulators (AOMs) in double-pass configuration, driven by an arbitrary waveform generator (Signadyne), to create the necessary pulse sequences. The beams are then carried with polarization-maintaining single-mode optical fibers to another optical table where the cryostat is located. The maximum available optical powers are about 20 mW, 3.5 mW and $150 \mu\text{W}$ for control, filter preparation, and input modes, respectively, measured in front of the cryostat. The frequency of the 606 nm laser is stabilized by Pound-Drever-Hall technique to a home-made temperature controlled Fabry-Perot cavity housed in a vacuum chamber. The input light is linearly polarized close to the optical D_2 axis to maximize the interaction with the Pr^{3+} ions. The measured optical depth of the Pr^{3+} transition at 606 nm is about 7 for both memory and filter crystal. In both cases, the inhomogeneous linewidth is about 6 GHz. After the storage, the retrieved signal passes through different diffraction order modes (-1st and 1st) of two consecutive AOMs, acting as temporal gate before passing through the filter crystal. A diffraction grating (DG) is then used to filter the noise not resonant with the crystal. The retrieved signal is coupled with 60 % efficiency into a single-mode fiber for connection to the single photon detector (SPD, PicoQuant τ SPAD-20, detection efficiency $\eta_d = 60\%$, dark count rate ~ 10 Hz). The total transmission of the input beam from the cryostat to the SPD is about 13 %

We tailor the AFC using optical pumping techniques as described in [31, 38]. We isolate a single class of atoms [39, 40] and create a 3.5 MHz wide AFC with $\Delta = 200$ kHz on the $1/2_g - 3/2_e$ transition within a 14 MHz wide transparency window (see Supplemental Material for details and for a comb example). During the preparation of the memory, the population removed from the comb is stored in the auxiliary $5/2_g$ state, while the $3/2_g$ is emptied. To further remove unwanted residual population in the $3/2_g$ state, we apply an extra series of 100 pulses on the $3/2_e - 3/2_g$ transition after the comb preparation. We then start the single-photon-level storage measurements. Weak gaussian input pulses with full width at half maximum (FWHM) duration of 430 ns and mean photon number μ_{in} are mapped on the AFC and transferred to spin-waves thanks to a strong control pulse. The control pulses have a Gaussian temporal profile with FWHM of 700 ns and are spectrally chirped by 5 MHz about the $3/2_e - 3/2_g$ transition. For each comb preparation, 1000 storage trials are performed with a repetition rate of ~ 7 kHz. The full cycle has a period of 700 ms, including memory preparation and light storage. It is synchronized with the cryostat cycle to reduce the effect of vibrations. The sequence is then repeated 500 to 1000 times to accumulate sufficient statistics.

Fig. 2(a) shows the time histograms of the retrieved photons with different μ_{in} . For this measurement, the

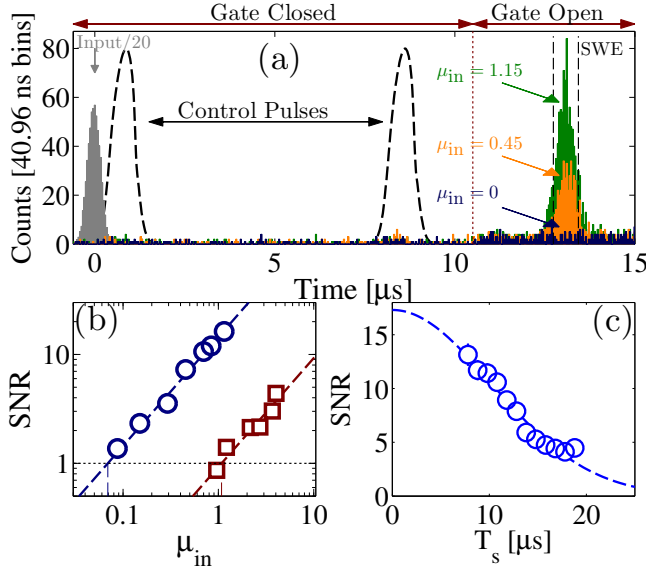


FIG. 2: (a). Time histograms of the retrieved photons measured for different input photon numbers when a transparency window 2 MHz wide is prepared in the filter crystal. The input ($\mu_{in} = 0.9$) and the control pulses, as measured in photon counting and from a reference photodiode (PD2 in Fig. 1), respectively, are also displayed. The chosen $0.7 \mu\text{s}$ wide detection window is indicated by the dashed lines about the three-level echo; it includes $\sim 80\%$ of the counts in the full echo mode. (b). Signal-to-noise ratio (SNR) as a function of the number of input photons for different filter width. Circles: 2 MHz; Squares: 14 MHz. The error bars (smaller than the data points) are evaluated with Poissonian statistics. The black dashed line indicates the limit of detection SNR = 1. The dotted lines are linear fits of the experimental data. Panel (c). Decay of the SNR as a function of the spin-wave storage time T_s with average photon number $\mu_{in} = 1$. From the fit with a Gaussian profile, the spin inhomogeneous broadening $\gamma_{in} = (26 \pm 1) \text{ kHz}$ can be extrapolated. By comparing the SNR that we measure at a storage time $T_s = 7.8 \mu\text{s}$ with the extrapolation at $T_s = 0 \mu\text{s}$, we can evaluate the decoherence term η_C to be about 75 %.

crystal filter has a hole width of 2 MHz. The spin-wave storage time is $T_s = 7.8 \mu\text{s}$, leading to a total storage time of $\tau_s = 1/\Delta + T_s = 12.8 \mu\text{s}$. From the trace with $\mu_{in} = 0$, we estimate an unconditional noise floor of $(2.0 \pm 0.3) \times 10^{-3}$ photons per pulse at the memory crystal. For $\mu_{in} = 1.15$, we measure $\text{SNR} = 16.3 \pm 2.4$. The linear scaling of the echo SNR with respect to increasing μ_{in} is shown with blue circles in Fig. 2(b). Typical values of efficiencies are $\eta_{AFC} = (5.6 \pm 0.3) \%$ and $\eta_{SW} = (2.8 \pm 0.1) \%$, from which we deduce $\eta_T = (81.7 \pm 2.6) \%$ (assuming $\eta_C \sim 75 \%$ [30]). A convenient figure of merit taking into account the noise and efficiency is given by the minimum μ_{in} necessary to detect a spin-wave echo with $\text{SNR} = 1$, called μ_1 . From the linear fit of the experimental data of Fig. 2(b), we find $\mu_1 = 0.069 \pm 0.002$. We then vary τ_s by changing T_s with $\mu_{in} = 1$, as shown in Fig. 2(c). The decay in the

SNR is compatible with a spin inhomogeneous broadening of $\gamma_{in} = (26 \pm 1) \text{ kHz}$, similar to previous measurements with bright pulses [29, 30]. We still observe $\text{SNR} = 4.5 \pm 0.4$ for $T_s = 18.8 \mu\text{s}$ ($\tau_s = 23.8 \mu\text{s}$).

We can estimate the contribution of the filter crystal in the suppression of the noise by preparing a wider transparency window. For a filter width of 14 MHz (squares in Fig. 2(b)) there is no filtering at the control frequency, and we observe an increase of the noise floor to $(2.3 \pm 0.6) \times 10^{-2}$ together with a slightly higher retrieval efficiency ($\eta_{SW} = (2.9 \pm 0.2) \%$), which results in μ_1 values up to about 1. When the filter crystal is bypassed, the noise floor raises to (0.23 ± 0.01) , indicating that the inhomogeneously broadened absorption profile of Pr^{3+} also contributes to partially filter the noise [26]. Nonetheless, for this set of measurements, we were able to achieve higher storage efficiency, i.e. $\eta_{SW} = (5.3 \pm 0.5) \%$, leading to a limited increase of the μ_1 to about 4.

For applications in QIS, it is crucial that the optical memory preserves the coherence of the stored qubits. We take advantage of the intrinsic temporal multimodality of the AFC protocol to demonstrate the phase preservation in the spin-wave storage of time-bin qubits. This type of encoding is widely used in quantum communication as it is robust against decoherence in optical fibers [34]. The time-bin qubits are expressed as $|\psi_{in}\rangle = c_1|e\rangle + c_2e^{i\Delta\alpha}|l\rangle$, where $|e\rangle$ ($|l\rangle$) represents a qubit in the early (late) time-bin, $\Delta\alpha$ is their relative phase, and $c_1^2 + c_2^2 = 1$. In order to store time-bin qubits, the duration of the input pulses is reduced (from 430 to 260 ns), leading to a reduction of η_{SW} to about 2.2 % and to an increase of the μ_1 up to $\mu_{1p} = 0.11 \pm 0.01$. We start by evaluating the fidelity of the states $|e\rangle$ and $|l\rangle$, located at the poles of the Bloch sphere, F_e and F_l , by storing only the early and the late qubits. We obtain average fidelity values for the poles ranging from $F_{el} = 85 \%$ to 98 % for photon number per qubit, μ_q , going from 0.6 to 5.9 (see Supplemental Material).

We then store superposition states located on the equator of the Bloch sphere. We use the memory itself to analyze the retrieved qubits [31] applying two partial write pulses as depicted in Fig. 3(a). This method provides a convenient way of analyzing time-bin qubits, but has the drawback of reducing the storage efficiency. As a matter of fact, in order to insert two write pulses, their duration needs to be reduced, which decreases their efficiency. Fig. 3(b) reports examples of interference fringes for $\mu_q = 1.5$. From sinusoidal fits, we obtain a raw mean visibility of $V_{+-} = (72.5 \pm 1.3) \%$. The fidelity of the process is calculated from the visibility, as $F = (1 + V)/2$ [34]. Finally, we obtain a total conditional fidelity per retrieved qubit $F_T = \frac{1}{3}F_{el} + \frac{2}{3}F_{+-}$, where F_{el} (F_{+-}) is the average fidelity over the poles (equator) basis. The obtained values are reported in Fig. 4 for different μ_q . We observe that the fidelity decreases with μ_q . To explain this behavior, we fit our data with a simple model

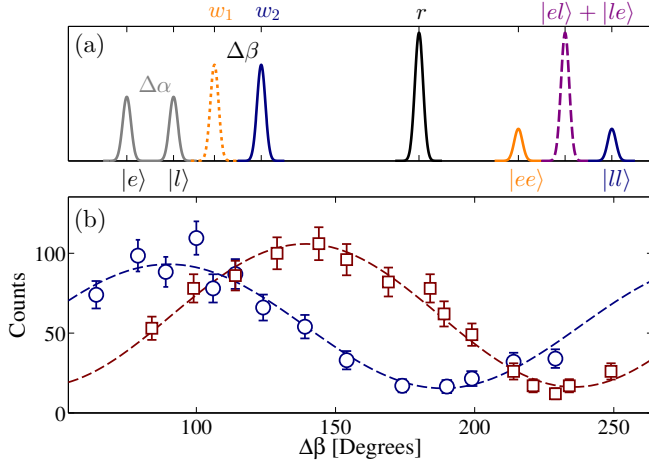


FIG. 3: (a) Pulse sequence to measure the time-bin qubit coherence. We apply two partial write pulses with a relative phase $\Delta\beta$ in order to split each pulse into two temporally separated echoes. If the delay between the time-bins $|e\rangle$ and $|l\rangle$ is equal to the time difference between the two write pulses, we can overlap the late echo of the early bin, $|el\rangle$, with the early echo of the late bin, $|le\rangle$. The output of the memory (occurring after the single read pulse r) has three time-bins, $\{|ee\rangle, |el\rangle + |le\rangle, |ll\rangle\}$. An interference will occur in the central time-bin if the coherence is preserved. The input pulses, located at $|e\rangle$ and $|l\rangle$ have a relative phase difference of $\Delta\alpha$. (b) Interference fringes obtained integrating over the central output time-bin (in this case $\Delta t_d = 0.5 \mu\text{s}$) as a function of the relative phase difference $\Delta\beta$ for $\mu_q = 1.5$. Circles: $\Delta\alpha = 90^\circ$, $V = (71.6 \pm 6.8) \%$; Squares: $\Delta\alpha = 135^\circ$, $V = (73.4 \pm 3.5) \%$.

taking into account the decrease of SNR with μ_q and the reduced efficiency due to the double write protocol (see Supplemental Material). The good agreement between the simple model and the data provides evidence that the decrease of fidelity is only due to the noise created by the control pulses, and not to a loss of coherence.

In order to infer the quantum nature of our memory, the total fidelity is compared with the highest fidelity achievable with a classical measure-and-prepare approach (solid curve in Fig. 4) taking into account the Poissonian statistics of the input states and the finite memory efficiency (2.2%) [4, 9, 23]. The experimental data are higher than the classical limit by more than one standard deviation for most μ_q investigated. With the raw data, the memory is in the quantum regime for $\mu_q > 0.96$. When correcting for the loss of efficiency in the analysis (which could be achieved by analyzing the qubits with an external interferometer), the model predicts that the quantum regime would be reached for $\mu_q > 0.25$ (see Supplemental Material).

The very low noise probability and the ability to obtain $\mu_1 \ll 1$ opens prospects for the spin-wave storage of single-photons, as required for many applications in QIS. In that case, the probability to have a photon before the memory (i.e including all optical loss between source and

memory) needs to be higher than μ_1 to enter the quantum regime. In the current experiment, the storage efficiency is limited by the available comb optical depth in our 3 mm long crystal, by the limited transfer efficiency ($\eta_T^2 = (67 \pm 4) \%$) and by technical issues (cryostat vibrations, laser linewidth, see Supplemental material). Note that much higher efficiencies (for storage in the excited state) have been obtained in $\text{Pr}^{3+}:\text{Y}_2\text{SiO}_5$ using longer crystal (69 %) [14] or impedance matched cavities (58 %) [41]. Longer storage times can also be achieved with dynamical decoupling techniques to counteract decoherence in the spin state [32, 33, 42, 43].

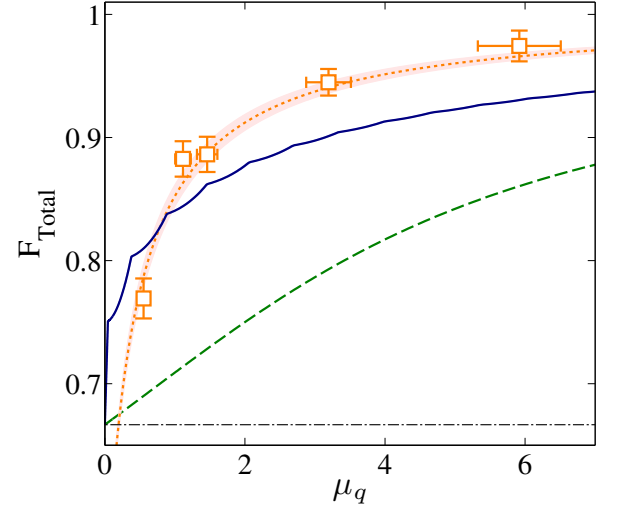


FIG. 4: Total fidelity vs input photon number per qubit, μ_q . The light orange squares are the data points with an error bar of 1 standard deviation. The orange dotted line is a fit to the data points using Eq. (5) in the Supplemental material, with the corresponding shaded area being the 1 standard deviation of the error in this fit. The solid blue (dashed green) line is the classical limit obtained by a measure and prepare strategy for our memory efficiency of $\eta_{\text{SW}} = 2.2 \%$ ($\eta_{\text{SW}} = 100 \%$) when testing the memory with weak coherent states [23]. The dash-dotted line is the classical limit for testing the memory with a single-photon Fock state ($F = 2/3$).

In conclusion, we demonstrated the spin-wave storage and on-demand retrieval of weak coherent states at the single-photon level in a solid state memory based on a $\text{Pr}^{3+}:\text{Y}_2\text{SiO}_5$ crystal. We achieved a SNR higher than 10 for single-photon level input pulses. Finally, we confirmed the quantum nature of our memory by storing time-bin qubits encoded in weak coherent states and demonstrating conditional fidelities for the retrieved qubits higher than what is possible with classical memories. These results open the door for long-lived storage and on-demand readout of non-classical light states in solid state devices and represent an important step in view of using solid state quantum memories in scalable quantum architectures.

Acknowledgements. We acknowledge financial sup-

port by the ERC starting grant QuLIMA, by the Spanish Ministry of Economy and Competitiveness (MINECO) and the Fondo Europeo de Desarrollo Regional (FEDER) through grant FIS2012-37569, by the European project CHIST-ERA QScale and by the People Programme (Marie Curie Actions) of the EU FP7 under REA Grant Agreement No. 287252.

Supplemental Material

In the supplemental material we report details on the atomic frequency comb preparation (section I.), the chosen strategy to suppress the technical noise (section II.), the characterization of the filter cristal (section III.), and, finally, we describe a theoretical model for the fidelity of the spin-wave storage of time-bin qubits (section IV.).

Atomic Frequency Comb Preparation

To prepare the atomic frequency comb (AFC) we follow the approach already described in [31, 38]. The frequency of the strong beam is firstly scanned by 14 MHz in 100 ms to create a wide transparency window (also referred to as pit) in the Pr^{3+} absorption line by spectral hole burning (curve a in Fig. 5). Afterwards a 2 MHz-wide sweep is operated outside the pit to pump the atoms back to the $1/2_g$ state. This creates a 3.5 MHz-wide absorbing feature corresponding to the $1/2_g - 3/2_e$ transition inside the pit, but also populates the $3/2_g$ state which in principle must be empty for later transfer of the input field (see Fig. 1(b) in the main text). Thus, a clean pulse with duration of 50 ms is applied on $3/2_g - 3/2_e$ transition to empty this ground state. The clean pulse also contributes to suppress the transitions of different classes of Pr^{3+} ions which might be addressed by the preparation pulses [44]. Then, a sequence of single-frequency hole-burning pulses is applied on the single class absorption feature resonant with the $1/2_g - 3/2_e$ transition, each time changing the frequency by a fixed amount, Δ . This sequence burns periodically spaced holes in the absorbing feature corresponding to the $1/2_g - 3/2_e$ transition and anti-holes at the frequency of the $3/2_g - 3/2_e$ transition, so a short burst of clean pulses is applied to maintain the $3/2_g$ state empty. For the AFC preparation it is crucial to have a third ground state ($5/2_g$) to use as auxiliary state where to store the excess of population resulting from the optical pumping. An example of the resulting comb structure for $\Delta = 200$ kHz is shown in Fig. 5, curve b. With the described procedure we are able to tailor absorption peaks as narrow as (43 ± 3) kHz, with a comb optical depth $d = 4.5 \pm 0.1$ and background optical depth $d_0 = 0.75 \pm 0.04$. It is worth noting that the limited dynamical range of the detector might fix a higher bound for the detected peak amplitude and thus lead to an overestimated full width at half maximum. When the memory is characterized with classical pulses, we find typical efficiency values of $\eta_{AFC} = (10.3 \pm 1.4)\%$ and $\eta_{SW} = (4.4 \pm 0.1)\%$. The prediction for gaussian AFC peaks is $\eta_{AFC} = \tilde{d}^2 e^{-\tilde{d}} e^{-7/F^2} e^{-d_0}$, where

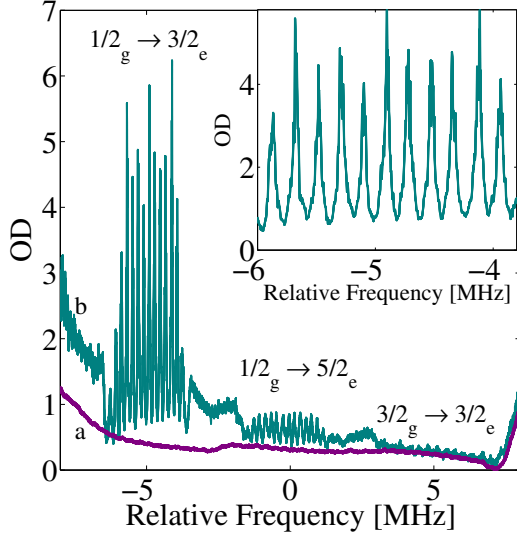


FIG. 5: Example of transparency window (curve a) and comb trace prepared with $\Delta = 200$ kHz (curve b). The inset shows a magnification of the comb corresponding to the $1/2_g - 3/2_e$ transition.

$\tilde{d} = d/F$ is the effective comb optical depth [21]. The measured value of η_{AFC} is compatible with the prediction, $\eta_{AFC,th} = (12.2 \pm 1.6) \%$, for the measured values of $d = 4.5 \pm 0.1$, $F = 4.7 \pm 0.4$ and $d_0 = 0.75 \pm 0.04$. For the same optical depth of our comb but assuming $d_0 = 0$, the model predicts a maximal efficiency of $\eta_{AFC,th} = 26.5 \%$ for a finesse of $F = 4$. Note that an even higher efficiency, $\eta_{AFC,th} = 34.8 \%$, is expected for square shaped comb peak and a finesse of $F = 3.2$ ([45]). In our case, the achievable contrast is limited by technical reasons, such as vibrations of the cryo-cooler and finite linewidth of the laser. When measured in photon counting mode, the efficiency is further reduced by the coincidence window taken (containing $\sim 80 \%$ of the total counts), by loss in the narrow-band filter ($\sim 10 \%$) and by instabilities due to long integration times ($\sim 10 \%$ loss).

Filtering

To achieve a low noise floor, $(2.0 \pm 0.3) \times 10^{-3}$, we use spatial, temporal and spectral filtering. As for the spatial filtering, the control and input beams are sent to the memory with a small angle, leading to an extinction of 10^{-5} . Temporal filtering is achieved thanks to a temporal gate implemented with two AOMs. It allows us to block the leakage of the strong control beams in the signal mode. This is important not to blind the single-photon detectors, but also to avoid burning a spectral hole in the crystal filter. A diffraction grating is employed to decrease the noise originated from incoherent fluorescence. The narrow-band spectral filter is prepared simultaneously with the AFC. The frequency of the filter

mode (shown in dashed red line in Fig. 1(a)) is scanned by 1.2 MHz around the input light frequency for 100 ms which results in a transparency window of around 2 MHz due to the power broadening effect. In order to temporally discriminate the stored and retrieved weak pulses from the portion of the FID leaking in the echo mode and happening at short time scales (a few μs), the optimization of the excited state storage efficiency at long storage times is crucial. By carefully optimizing the storage times, in both the excited and ground states, and the pulse durations a compromise can be reached between the noise level and a reasonable retrieval efficiency.

Filter crystal characterization

We provide in this section details about the noise suppression realized by the filter crystal. The main advantage of using a second crystal is that it provides a dynamical filter, whose center frequency and bandwidth can be easily tuned, as it is obtained by spectral hole burning.

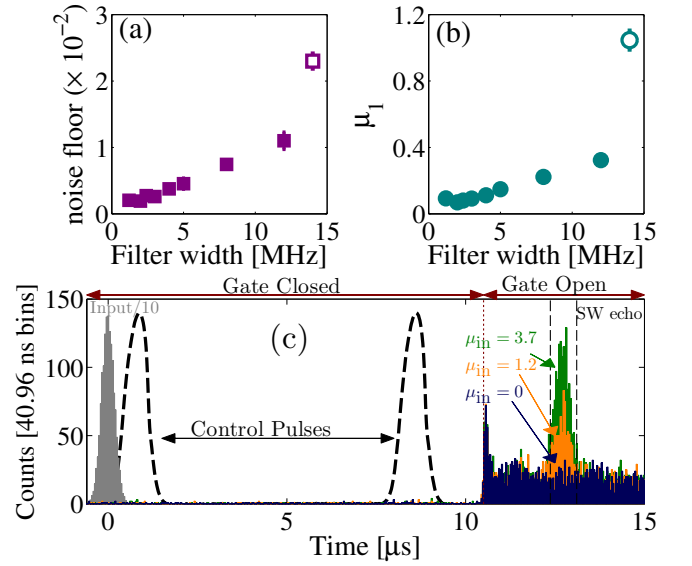


FIG. 6: Noise floor in the echo window (a) and μ_1 (b) value as a function of the spectral hole width in the filter crystal. Filled symbols: hole centered at the input pulse frequency; open symbols: transparency window coincident with that prepared in the memory crystal (see curve b in Fig. 5). (c) Time histogram of the retrieved photons for different input photon numbers, μ_{in} , and a filter width of 14 MHz. The input ($\mu_{in} = 0.9$) and the control pulses (measured with a reference photodetector) are also displayed.

Fig. 6(a) represents the noise floor (noise counts per pulse at the memory crystal) as evaluated from noise measurements where we burn in the filter crystal spectral holes of different width centered about the input pulse frequency (solid symbols). The noise in the echo window increases by one order of magnitude when the filter

width increases from 0.8 to 12 MHz. The open symbol refers to the extreme case of a 14 MHz-wide transparency window coincident with the one prepared in the memory crystal to host the AFC (see curve a in Fig. 5). Here the noise floor is further doubled because the transparency window allows the control pulse frequency to pass by and reach the detector. The increase in the noise affects consequently the μ_1 value as shown in Fig. 6(b). Nevertheless, this value also depends on the echo counts, thus the narrowest filter width does not necessarily correspond to the best case. As a matter of fact, the best μ_1 value is measured for a filter width which allow the major portion of the echo signal to pass by but suppresses efficiently the noise at the control pulse frequency, i.e. 2 MHz. The value of μ_1 also depends on the echo efficiency and is thus more affected by power fluctuations than the noise floor. We believe this is the reason why its increase in the case of totally open transparency window is more pronounced than that of the noise floor (compare filled and open symbols in panel (a) and (b) of Fig. 6). Panel (c) of Fig. 6 shows the time histogram of the retrieved photons for different input photon numbers in the case of a 14 MHz-wide pit prepared in the filter crystal. Finally we evaluate the extinction ratio of our 2 MHz-wide spectral filter by switching off the AFC and sending input pulses through the transparency window in the memory crystal firstly resonant with the filter center, then at the control pulse frequency. By comparing the total counts reaching the detector in the two cases, we estimate the extinction ratio to be about 750.

Modeling the Fidelity

Fig. 4 from the main document shows the measured total fidelity as a function of the mean photon number per qubit, μ_q , with a corresponding fit using the model we develop in this section. The aim of the model is to show that the reduction of the fidelity as the photons per qubit are reduced is entirely due to the noise of the memory and not due to a loss of coherence caused by e.g. phase noise in the laser. The goal of our model is to express the total fidelity as a function of the same μ_1 parameter.

Firstly, let us look at the output of the memory for the two differing measurements, namely the measurement of the $|e\rangle$ or $|l\rangle$ qubit (i.e. the poles of the Bloch sphere) and the measurement of the coherence between $|e\rangle$ and $|l\rangle$ (i.e. the equator of the Bloch sphere). The former (latter) are schematically depicted in Fig. 7(a) (7(b)).

For a given integration width, we sum over both E and L for the poles measurement, while for the coherence measurement we integrate over the window labelled E-L+L-E (see figure 7(b)).

Consider the example depicted in Fig. 7(a), where the $|e\rangle$ qubit has been stored and then recalled. We label the

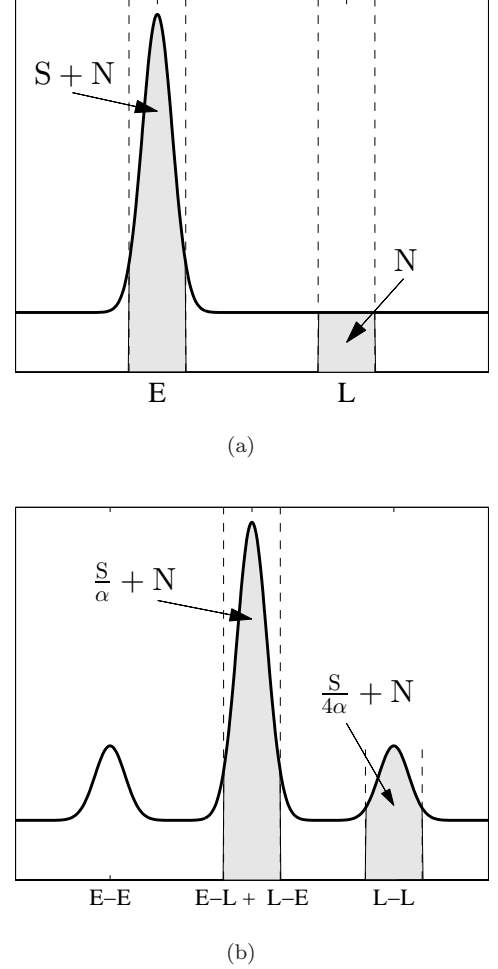


FIG. 7: (a) Schematic example of the memory output for storage of an $|e\rangle$ qubit. (b) Schematic example of the memory output for storage of an $|e\rangle + |l\rangle$ where the relative phases are such that the maximum interference is observed.

integrated counts in the window about E as $S + N$ and the integrated counts about the window L as N , where S is the signal (not including the noise) and N is the noise. Then, the fidelity is the ratio of the counts in E to the total counts over E and L, i.e.

$$\mathcal{F}_e = \frac{S + N}{S + N + N} = \frac{S/N + 1}{S/N + 2} = \frac{\text{SNR} + 1}{\text{SNR} + 2}. \quad (1)$$

where SNR is the signal to noise ratio. Provided the efficiency and noise are the same for storing the $|l\rangle$ qubit, $\mathcal{F}_l = \mathcal{F}_e = \mathcal{F}_{el}$. Finally, we can express the above fidelity as a function of the μ_1 of this measurement (see main text for definition) by noting that $\text{SNR} = \mu_q/\mu_{1p}$, where μ_{1p} is the μ_1 characteristic of the poles measurement. The expression for the fidelity becomes

$$\mathcal{F}_{el} = \frac{\mu_q + \mu_{1p}}{\mu_q + 2\mu_{1p}}. \quad (2)$$

and we measure $\mu_{1p} = 0.11 \pm 0.01$.

Now let us consider Fig. 7(b), which depicts an arbitrary qubit $|e\rangle + |l\rangle$ being recalled, and the relative phases are such that the maximum interference is observed. Firstly, the integrated counts corresponding to the window at the time labelled E-E are $S/4\alpha + N$ where the signal S is the same as defined earlier. Here, the signal S is reduced by a factor of 4, this is because the number of photons per qubit are distributed equally within the input time-bins (factor of 2) and the echo is distributed equally between the output time-bins (factor of 2). The factor α reduction in the signal is because we use different bandwidth pulses for the double write process which gives a reduced efficiency in the echo. The amount of signal in the window E-L + L-E is 4 times that of the signal in the L-L window provided the interference is fully coherent (note the same is true for the E-E window). The resulting counts are then $S/\alpha + N$. It is worth noting that if we instead used an unbalanced Mach Zehnder interferometer, we would have no reduction in the signal and $\alpha = 1$.

The fidelity of the coherence measurement is obtained from the visibility of the interference fringe by $\mathcal{F} = (1 + V)/2$ [34] where the visibility V is defined as

$$\begin{aligned} V &= \frac{\max - \min}{\max + \min} = \frac{S/\alpha + N - N}{S/\alpha + N + N} \\ &= \frac{S}{S + 2N\alpha} = \frac{\text{SNR}}{\text{SNR} + 2\alpha} \end{aligned} \quad (3)$$

where max (min) refers to the maximum (minimum) integrated counts of the fringe, the max being $S/\alpha + N$ and min being N . Note that we have V in terms of the SNR of the poles measurement, so the resulting fidelity can be written in terms of μ_{1p} , i.e.

$$\mathcal{F}_{+-} = \frac{1}{2} + \frac{1}{2} \frac{\mu_q}{\mu_q + 2\alpha\mu_{1p}}, \quad (4)$$

where the subscript $+(-)$ refers to the qubit $|e\rangle \pm |l\rangle$ ($|e\rangle \pm i|l\rangle$), and we assume $\mathcal{F}_+ = \mathcal{F}_- = \mathcal{F}_{+-}$. We measure α by comparing the μ_1 in the L-L window of figure 7(b) to μ_{1p} and we get $\alpha = 2.5 \pm 0.6$.

Now, the total fidelity is given by $\mathcal{F}_T = \frac{1}{3}\mathcal{F}_{el} + \frac{2}{3}\mathcal{F}_{+-}$, which leads to

$$\mathcal{F}_T = \frac{1}{3} \left[\frac{\mu_q + \mu_{1p}}{\mu_q + 2\mu_{1p}} \right] + \frac{1}{3} \left[1 + \frac{\mu_q}{\mu_q + 2\alpha\mu_{1p}} \right], \quad (5)$$

concluding our simple model for the fidelity. Taking the measured μ_{1p} , we fit the data in Fig. 8 with equation 5 having α as a free parameter. We get $\alpha = 2.5 \pm 0.3$ which agrees excellently with the measured value stated earlier. We therefore can conclude that the reduction of the fidelity is due to the noise on the output of the memory and not phase noise. For $\mu_q > 0.96$ the fidelity surpasses the classical bound, remaining in the quantum regime. Also in Fig. 8 we plot the case for $\alpha = 1$ for

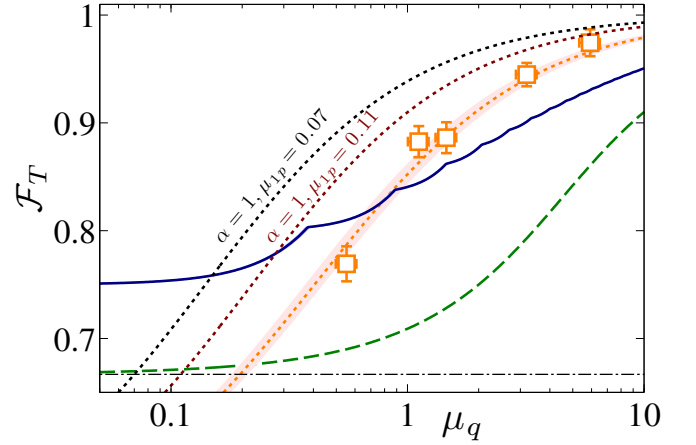


FIG. 8: Total fidelity vs input photon number per qubit. The light orange squares are the data points with an error bar of 1 standard deviation. The light orange dotted line is a fit to the data points using eq. 5 with μ_{1p} fixed at 0.11 and $\alpha = 2.5 \pm 0.3$. The corresponding shaded area is the 1 standard deviation of the error in this fit. The solid blue (dashed green) line is the classical limit obtained by a measure and prepare strategy and a memory efficiency of $\eta_{3LE} = 2.2\%$ ($\eta_{3LE} = 100\%$) when testing the memory with weak-coherent states [4, 23]. We see that for $\mu_q > 0.96$ the fidelity is above the classical benchmark. We show also the case of $\alpha = 1$ and $\mu_{1p} = 0.11$, i.e. the case where our detection of the coherence is replaced by an unbalanced Mach Zehnder interferometer for example. Furthermore, we show the case of $\alpha = 1$ and $\mu_{1p} = 0.07$, i.e. the μ_1 measured for the optimised pulse bandwidth case. The dash-dotted line is the classical limit for testing the memory with a single-photon Fock state ($\mathcal{F} = 2/3$).

$\mu_{1p} = 0.11$ and $\mu_{1p} = 0.07$ (the case shown in Fig. 2 of the main text). The fidelity exceeds the classical bound for photon numbers much less than 1 for these cases.

For completeness, we include table I which shows all the measured fidelities for every μ_q tested. Also, we include examples of the output of the memory for early and late inputs (Fig. 9(a)) and for the input $|e\rangle + |l\rangle$ where the phase of the double-write process is adjusted to show maximum and minimum interference in the E-L + L-E window.

μ_q	\mathcal{F}_{el}	\mathcal{F}_{+-}	\mathcal{F}_T	\mathcal{F}_C
5.9	$(97.9 \pm 1.5)\%$	$(97.2 \pm 1.7)\%$	$(97.4 \pm 1.2)\%$	$(93.0 \pm 0.1)\%$
3.2	$(96.9 \pm 2.2)\%$	$(93.3 \pm 1.2)\%$	$(94.5 \pm 1.1)\%$	$(90.1 \pm 0.1)\%$
1.5	$(93.5 \pm 2.9)\%$	$(86.2 \pm 1.6)\%$	$(88.6 \pm 1.4)\%$	$(86.2 \pm 0.1)\%$
1.1	$(93.3 \pm 3.1)\%$	$(85.8 \pm 1.5)\%$	$(88.3 \pm 1.4)\%$	$(84.4 \pm 0.1)\%$
0.6	$(84.9 \pm 4.2)\%$	$(72.9 \pm 1.3)\%$	$(76.9 \pm 1.6)\%$	$(81.0 \pm 0.1)\%$

TABLE I: Fidelities \mathcal{F}_{el} , \mathcal{F}_{+-} and \mathcal{F}_T for each μ_q tested. \mathcal{F}_C is the classical benchmark for testing the device with weak coherent states which depends on the efficiency of the memory and the input photon number used [4, 23]. The stated errors are one standard deviation.

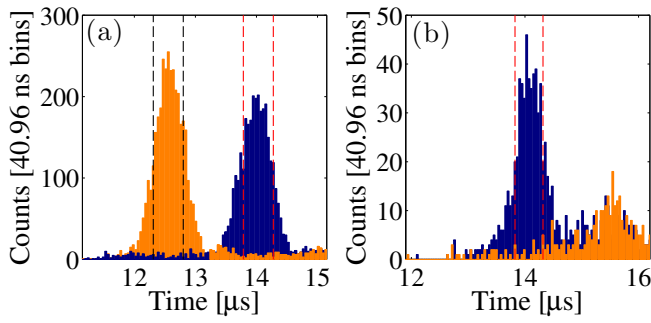


FIG. 9: (a) An example of the detected counts at the output of the memory for the early (light orange histogram) and late (dark blue histogram) input qubits with $\mu_q = 3$. The vertical dashed lines correspond to the $0.5 \mu\text{s}$ integration windows for the calculation of the fidelity. (b) An example of detected counts at the output of the memory for an input qubit $|e\rangle + |l\rangle$ with $\mu_q = 5.9$. The dark blue (light orange) histogram shows the case when the relative phase of the double-write process is such that the interference is maximized (minimized) in the integration window (indicated by the vertical dashed line). The pulse feature on the right corresponds to the L-L window of Fig. 7(b) while the E-E window is not detected here as the temporal gate is closed to negate the effects of the control pulses.

* Present address: Department of Physics, Clarendon Laboratory, University of Oxford, Oxford OX1 3PU, United Kingdom

† Electronic address: margherita.mazzera@icfo.es

- [1] L.-M. Duan, M. D. Lukin, J. I. Cirac, and P. Zoller, *Nature* **414**, 413 (2001).
- [2] N. Sangouard, C. Simon, H. de Riedmatten, and N. Gisin, *Rev. Mod. Phys.* **83**, 33 (2011).
- [3] E. Knill, R. Laflamme, and G. J. Milburn, *Nature* **409**, 46 (2001).
- [4] H. P. Specht *et al.*, *Nature* **473**, 190 (2011).
- [5] C. W. Chou *et al.*, *Nature* **438**, 828 (2005).
- [6] T. Chanelière *et al.*, *Nature* **438**, 833 (2005).
- [7] K. S. Choi, H. Deng, J. Laurat, and H. J. Kimble, *Nature* **452**, 67 (2008).
- [8] H. Zhang *et al.*, *Nat Photon* **5**, 628 (2011).
- [9] A. Nicolas *et al.*, *Nat Photon* **8**, 234 (2014).

- [10] B. Julsgaard *et al.*, *Nature* **432**, 482 (2004).
- [11] M. Hosseini *et al.*, *Nat Phys* **7**, 794 (2011).
- [12] M. Sprague *et al.*, *Nat Photon* **8**, 287 (2014).
- [13] H. de Riedmatten *et al.*, *Nature* **456**, 773 (2008).
- [14] M. P. Hedges, J. J. Longdell, Y. Li, and M. J. Sellars, *Nature* **465**, 1052 (2010).
- [15] C. Clausen *et al.*, *Nature* **469**, 508 (2011).
- [16] E. Saglamyurek *et al.*, *Nature* **469**, 512 (2011).
- [17] E. Togan *et al.*, *Nature* **466**, 730 (2010).
- [18] H. Bernien *et al.*, *Nature* **497**, 86 (2013).
- [19] D. G. England *et al.*, arXiv:1409.2892 (2014).
- [20] R. M. Macfarlane, *J. Lumin.* **100**, 1 (2002).
- [21] M. Afzelius, C. Simon, H. de Riedmatten, and N. Gisin, *Phys. Rev. A* **79**, 052329 (2009).
- [22] N. Sinclair *et al.*, *Phys. Rev. Lett.* **113**, 053603 (2014).
- [23] M. Gündoğan *et al.*, *Phys. Rev. Lett.* **108**, 190504 (2012).
- [24] C. Clausen, F. Bussi eres, M. Afzelius, and N. Gisin, *Phys. Rev. Lett.* **108**, 190503 (2012).
- [25] Z.-Q. Zhou *et al.*, *Phys. Rev. Lett.* **108**, 190505 (2012).
- [26] D. Riel ander *et al.*, *Phys. Rev. Lett.* **112**, 040504 (2014).
- [27] I. Usmani *et al.*, *Nat Photon* **6**, 234 (2012).
- [28] F. Bussi eres *et al.*, *Nat Photon* **8**, 775 (2014).
- [29] M. Afzelius *et al.*, *Phys. Rev. Lett.* **104**, 040503 (2010).
- [30] M. G ndo an *et al.*, *New Journal of Physics* **15**, 045012 (2013).
- [31] N. Timoney *et al.*, *Phys. Rev. A* **88**, 022324 (2013).
- [32] J. J. Longdell, E. Fraval, M. J. Sellars, and N. B. Manson, *Phys. Rev. Lett.* **95**, 063601 (2005).
- [33] G. Heinze, C. Hubrich, and T. Halfmann, *Phys. Rev. Lett.* **111**, 033601 (2013).
- [34] I. Marcikic *et al.*, *Nature* **421**, 509 (2003).
- [35] P. Humphreys *et al.*, *Phys. Rev. Lett.* **111**, 150501 (2013).
- [36] H. Zhang *et al.*, *Applied Physics Letters* **100**, (2012).
- [37] S. E. Beavan, E. A. Goldschmidt, and M. J. Sellars, *J. Opt. Soc. Am. B* **30**, 1173 (2013).
- [38] N. Maring *et al.*, *New Journal of Physics* **16**, 113021 (2014).
- [39] M. Nilsson *et al.*, *Phys. Rev. B* **70**, 214116 (2004).
- [40] O. Guillot-No el *et al.*, *Phys. Rev. B* **79**, 155119 (2009).
- [41] M. Sabooni, Q. Li, S. Kr  ll, and L. Rippe, *Phys. Rev. Lett.* **110**, 133604 (2013).
- [42] M. F. Pascual-Winter, R.-C. Tongning, T. Chaneli ere, and J.-L. Le Gou et, *Phys. Rev. B* **86**, 184301 (2012).
- [43] M. Lovric, D. Suter, A. Ferrier, and P. Goldner, *Phys. Rev. Lett.* **111**, 020503 (2013).
- [44] O. Guillot-No el *et al.*, *Phys. Rev. B* **75**, 205110 (2007).
- [45] M. Bonarota, J. Ruggiero, J.-L. Le Gou et, and T. Chaneli ere, *Phys. Rev. A* **81**, 033803 (2010).